

See discussions, stats, and author profiles for this publication at: <https://www.researchgate.net/publication/228331114>

# A precursor route to single-crystalline WO<sub>3</sub> nanoplates with an uneven surface and enhanced sensing properties

ARTICLE *in* DALTON TRANSACTIONS · JULY 2012

Impact Factor: 4.2 · DOI: 10.1039/c2dt30748k · Source: PubMed

CITATIONS

21

READS

65

8 AUTHORS, INCLUDING:



**Xiaoxin Zou**

Jilin University

63 PUBLICATIONS 863 CITATIONS

SEE PROFILE



**Guo-Dong Li**

Jilin University

162 PUBLICATIONS 3,793 CITATIONS

SEE PROFILE



**Juan Su**

Centers for Disease Control and Prevention...

89 PUBLICATIONS 1,018 CITATIONS

SEE PROFILE



**Jun Zhao**

Hebei University of Science and Technology

28 PUBLICATIONS 393 CITATIONS

SEE PROFILE

A precursor route to single-crystalline WO<sub>3</sub> nanoplates with an uneven surface and enhanced sensing properties†Xiao-Xin Zou,<sup>a,b</sup> Guo-Dong Li,<sup>\*b</sup> Pei-Pei Wang,<sup>b</sup> Juan Su,<sup>a,b</sup> Jun Zhao,<sup>b</sup> Li-Jing Zhou,<sup>b</sup> Yu-Ning Wang<sup>a,b</sup> and Jie-Sheng Chen<sup>\*a</sup>

Received 5th April 2012, Accepted 6th June 2012

DOI: 10.1039/c2dt30748k

A W-containing inorganic–organic nanohybrid with a plate-like morphology has been successfully prepared through a nonaqueous synthetic route using WCl<sub>6</sub> as the tungsten source and benzyl alcohol as the solvent. The as-prepared hybrid nanomaterial was used directly as an efficient precursor for the formation of WO<sub>3</sub> nanoplates *via* a simple thermal treatment process. The as-obtained WO<sub>3</sub> material maintains the plate-like morphology of the precursor and possesses a unique uneven surface structure. It is noted that the use of a inorganic–organic hybrid precursor is essential for the creation of an uneven surface on the WO<sub>3</sub> nanoplates, which exhibit high sensitivity and selectivity for the detection of acetone vapour at a relatively low operating temperature (200 °C). The excellent sensing performance of the WO<sub>3</sub> nanomaterial is attributed to its unique uneven surface structure besides the small particle size and ultrathin morphology.

## 1. Introduction

One of the ongoing interests in material research concerns the chemistry and physics of inorganic–organic hybrid nanomaterials.<sup>1</sup> The integration of the two (inorganic and organic) components at a nanometer scale leads to the formation of new materials that possess enhanced and/or combined properties originating from individual components, and even novel functionalities that are not available to the individual components alone. To date, many efforts have been devoted to the design and synthesis of new inorganic–organic hybrid nanomaterials, and a great deal of advances have been seen in organoamine–chalcogenide nanohybrids,<sup>2</sup> organoamine–metal oxide nanohybrids<sup>3</sup> and alcohol–metal oxide nanohybrids.<sup>4</sup> With the integration of inorganic and organic components, these nanohybrids exhibit novel optical, electrical, and magnetic properties.<sup>1</sup> In the meantime, they have also been used as efficient precursors for the preparation of inorganic nanomaterials with various structures that cannot be readily acquired using other approaches. For instance, porous Cd<sub>x</sub>Zn<sub>1-x</sub>S nanosheets and hollow Cd<sub>x</sub>Zn<sub>1-x</sub>Se nanoframes were fabricated by the cation-exchange reaction of organoamine–chalcogenide nanohybrids with cadmium ions.<sup>5</sup> N-doped ZnS nanoparticles, porous ZnO nanosheets, Fe<sub>7</sub>S<sub>8</sub> nanowires and porous Fe<sub>2</sub>O<sub>3</sub> nanorods were prepared through

simple thermal treatment of organoamine–chalcogenide nanohybrids.<sup>6</sup> Some metal oxides, such as TiO<sub>2</sub>, SnO<sub>2</sub> and WO<sub>3</sub>, with particular nanostructures were obtained through thermal or light-driven transformation of the corresponding metal-based inorganic–organic nanohybrids.<sup>7</sup> These successes prompted us to explore new inorganic–organic hybrid nanostructures and to elucidate their potential application as an efficient precursor for the preparation of inorganic nanomaterials.

On the other hand, gas sensors based on semiconducting metal oxides have been extensively used to detect/monitor a wide variety of gases and organic vapors due to their thermal and environmental stability as well as good response reversibility.<sup>8</sup> The working principle of oxide gas sensors is primarily based on the variation of the electrical resistance, which results from the interaction process between the chemisorbed oxygen species on the sensor surface and the gas molecules to be detected. Since the discovery of the gas-sensing effect,<sup>9</sup> much effort has been made in order to improve the performance (such as sensitivity, selectivity, as well as response and recovery time) of oxide sensors. In view of the fact that sensing events occur on the surface of the oxide semiconductor, an effective strategy to enhance the gas-sensing properties is to increase the surface area and active sites by reducing the crystallite size down to the nanometer scale. The current nanoscience, in principle, will potentially offer devices with greater sensitivity, selectivity, and reliability than conventional sensors.<sup>8</sup> Nevertheless, achieving the above goal is not without challenges. The first challenge is the large-scale synthesis of nanostructures with a particular morphology from a controllable and reproducible chemical process. The second one is the establishment of a relationship between a particular nanostructure and its gas-sensing properties. The third one may be the further engineering of nanostructures at a smaller

<sup>a</sup>School of Chemistry and Chemical Engineering, Shanghai Jiao Tong University, Shanghai, 200240, P.R. China. E-mail: chemcj@sjtu.edu.cn

<sup>b</sup>State Key Laboratory of Inorganic Synthesis and Preparative Chemistry, College of Chemistry, Jilin University, Changchun, 130012, P.R. China. E-mail: lgd@jlu.edu.cn

† Electronic supplementary information (ESI) available: SEM images of the commercially available WO<sub>3</sub> sample. See DOI: 10.1039/c2dt30748k

scale to maximize their material properties. To deal with these challenges, new strategies for nanomaterial synthesis and a deep understanding of structure–property correlations should be actively pursued.

Tungsten trioxide ( $\text{WO}_3$ ), an indirect band gap semiconductor, is a well-established oxide material which has been employed as a promising candidate in gas-sensing applications.<sup>10–13</sup> Up to now, surface modification with noble metal particles (such as Ag, Au, Pt)<sup>10</sup> and bulk doping with heteroatoms (such as Cr, Si)<sup>11</sup> have been attempted to improve the sensing properties of  $\text{WO}_3$ . By comparison, the nanoscale design of  $\text{WO}_3$  material is a simpler and more cost-effective strategy, avoiding the high cost of noble metals and/or the complexity of multicomponent systems. Many efforts have been devoted to obtain nanosized  $\text{WO}_3$  materials for sensing applications, and the corresponding results indicate that the particle size and morphology of  $\text{WO}_3$  play an important role in its gas-sensing performance.<sup>12,13</sup> In this article, we demonstrate that the surface structure besides the particle size and morphology is another important factor in determining the gas-sensing properties of  $\text{WO}_3$ . In particular, a precursor route has been employed for the design of nano-scaled uneven surfaces on  $\text{WO}_3$  nanoplates using a W-containing inorganic–organic hybrid (designated W-IOH) as a starting material. The as-prepared  $\text{WO}_3$  material exhibits high sensitivity and selectivity for the detection of acetone vapour at a relatively low operating temperature (200 °C).

## 2. Experimental section

### Materials

Tungsten(vi) chloride ( $\text{WCl}_6$ ) was purchased from Aladdin Reagent Corporation (Shanghai, China). Benzyl alcohol (BA), pyrocatechol, ethanol and the reference  $\text{WO}_3$  sample were purchased from Tianjin Guangfu Fine Chemical Research Institute. All the reagents were of analytic grade and used as received without further purification. Deionized water was used throughout.

### Preparation of the W-IOH Precursor

The W-IOH precursor was prepared through a benzyl alcohol-mediated synthetic route. In a typical synthesis,  $\text{WCl}_6$  (1.2 g, 3 mmol) as the tungsten source and a small amount of pyrocatechol (50 mg, 0.45 mmol) were added to benzyl alcohol (60 mL) and stirred vigorously for 30 minutes at room temperature. The mixture was then heated at 80 °C for 50 h under stirring. After cooling to room temperature, the brown W-IOH precipitate was washed several times with ethanol and dried naturally at room temperature.

### Formation of $\text{WO}_3$ nanoplates with an uneven surface from W-IOH

The  $\text{WO}_3$  nanoplates with an uneven surface were obtained by simply calcining the W-IOH precursor in a muffle furnace at 450 °C for 2 h.

To determine the role of the organic component (benzene alcohol) in the W-IOH precursor in the creation of an uneven

surface on  $\text{WO}_3$  nanoplates, a light-driven approach was used to extract the organic component from W-IOH, as demonstrated in our previous reports.<sup>14</sup> Typically, irradiation of W-IOH under UV-light was performed in a water-cooled quartz cylindrical cell (see schematic drawing in Fig. S1†), which was illuminated from an internal light source with about a 1 cm optical path length. The UV-light source was a 125 W high-pressure mercury lamp and the irradiation intensity of the UV-light was about  $9.1 \times 10^4 \mu\text{W cm}^{-2}$ . The W-IOH precursor (1.0 g) was dispersed in water (100 mL) and then exposed to the UV-light irradiation for 5 h. After the irradiation, the solid sample was harvested and dried in air, and it was identified as  $\text{WO}_3 \cdot \text{H}_2\text{O}$  by XRD measurement. This  $\text{WO}_3 \cdot \text{H}_2\text{O}$  material was then calcined in a muffle furnace at 450 °C for 2 h to obtain another  $\text{WO}_3$  sample.

### General characterization

The powder X-ray diffraction (XRD) patterns were recorded on a Rigaku D/Max 2550 X-ray diffractometer using  $\text{Cu K}\alpha$  radiation ( $\lambda = 1.5418 \text{ \AA}$ ). The scanning electron microscope (SEM) images were taken on a JEOL JSM 6700F electron microscope. The transmission electron microscope (TEM) and high-resolution TEM (HRTEM) images were obtained on a JEOL JSM-3010 microscope. The FT-IR spectra were acquired on a Bruker IFS 66v/S FTIR spectrometer. The nitrogen adsorption and desorption isotherms were measured using a Micromeritics ASAP 2020M system. The Raman spectra were obtained with a Renishaw Raman system model 1000 spectrometer with a 20 mW air-cooled argon ion laser (514.5 nm) as the exciting source (the laser power at the sample position was typically 400  $\mu\text{W}$  with an average spot size of 1  $\mu\text{m}$  in diameter). The analysis of the organic species present in the UV-irradiation reaction system was performed on a Shimadzu GC-2014C gas chromatograph.

### Sensor fabrication and performance testing

The gas sensor was fabricated by pasting a viscous slurry of the obtained  $\text{WO}_3$  sample onto an alumina tube with a diameter of 1 mm and a length of 4 mm, which was positioned with a pair of Au electrodes and four Pt wires on both ends of the tube. A Ni–Cr alloy coil through the tube was employed as a heater to control the operating temperature. Gas sensing tests were performed on a commercial CGS-8 Gas Sensing Measurement System (Beijing Elite Tech Company Limited). The sensor sensitivity is defined as the ratio  $R_a/R_g$ , where  $R_a$  and  $R_g$  are the electrical resistances of the sensor in air and in the testing gas, respectively. The response and recovery time are defined as the time taken by the sensor to achieve 90% of the total resistance change in the case of adsorption and desorption, respectively. For comparison, the sensor performance of the commercially available  $\text{WO}_3$  sample was also tested.

## 3. Results and discussion

### 3.1 Preparation and characterization of the W-IOH precursor

The W-IOH precursor was prepared on a large scale through a benzyl alcohol-mediated nonaqueous synthetic route. In the

typical system,  $\text{WCl}_6$  functions as the tungsten source, and benzyl alcohol (BA) acts as the solvent but also as the reactive agent that entered the structure of W-IOH. The formation of W-IOH was confirmed by XRD measurement.<sup>15</sup> As shown in Fig. 1a, a set of diffraction peaks ( $2\theta > 20^\circ$ ), which are mainly indexed to  $\text{WO}_3 \cdot \text{H}_2\text{O}$ , appear in the pattern. In addition to these diffraction peaks related to  $\text{WO}_3 \cdot \text{H}_2\text{O}$ , a strong XRD peak at  $2\theta = 5.6^\circ$  and two relatively weak peaks at  $2\theta = 11.3$  and  $16.7^\circ$  are also observed, and these three peaks correspond to the d-spacing values of 1.57, 0.79, and 0.53 nm, respectively. The presence of these XRD peaks ( $2\theta < 20^\circ$ ) indicates the formation of meso-structures due to the self-assembly between the BA molecules and  $\text{WO}_3 \cdot \text{H}_2\text{O}$ . The structure of W-IOH was further confirmed by IR spectroscopy (Fig. 1b). A broad IR absorption due to stretching vibrations of hydroxyls (OH groups) and a relatively weak absorption due to bending vibration of hydroxyls are observed at approximately  $3397$  and  $1623 \text{ cm}^{-1}$ , respectively, indicating that a considerable amount of OH groups and water molecules exist in W-IOH. Several absorption bands associated with BA molecules are also observed in the IR spectrum between  $1200$  and  $1455 \text{ cm}^{-1}$ .<sup>15</sup> In addition, a very strong and broad IR band at  $688 \text{ cm}^{-1}$  is assigned to the stretching vibration of O–W–O, and two bands at  $941$  and  $989 \text{ cm}^{-1}$  are ascribed to

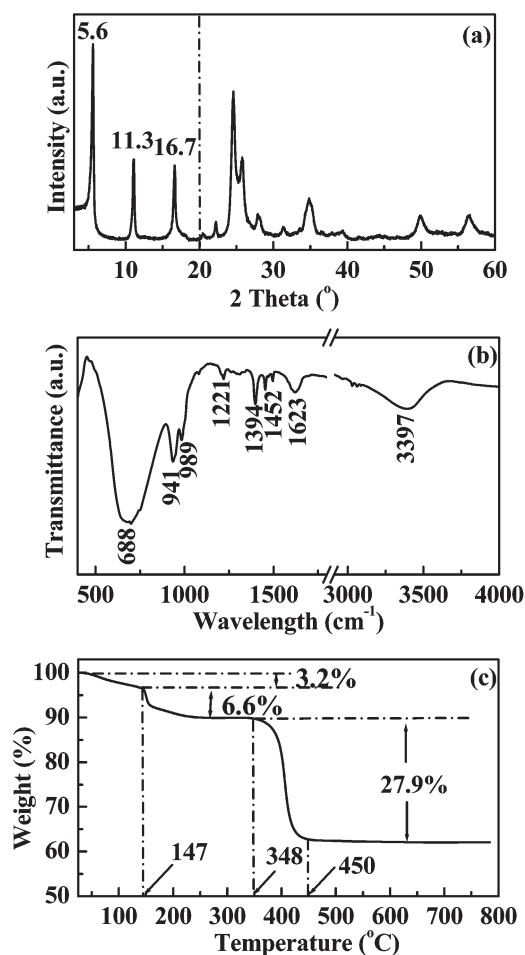


Fig. 1 XRD pattern (a) and IR spectrum (b) and TG curve (c) for the W-IOH precursor.

the stretching vibrations of  $\text{W}=\text{O}$ .<sup>15,16</sup> The thermogravimetric (TG) analysis for W-IOH was carried out in air from  $25$  to  $800^\circ\text{C}$  and the corresponding TG curve is shown in Fig. 1c. With the further increase in temperature from  $25$  to  $800^\circ\text{C}$ , the W-IOH precursor undergoes a small weight loss (3.2%) below  $147^\circ\text{C}$ , which is mainly due to the elimination of physically adsorbed water and organic molecules, and two sharp weight losses above  $147^\circ\text{C}$ . The first sharp weight loss (6.6%) takes place at  $147^\circ\text{C}$ , and this weight loss is attributed to the removal of water molecules in  $\text{WO}_3 \cdot \text{H}_2\text{O}$ . The second weight loss starts at  $365^\circ\text{C}$  and ends at about  $450^\circ\text{C}$ . A total weight loss of about 27.9% is observed, and this weight loss is originated from the decomposition of BA in the hybrid material. From the above weight loss values it is estimated that the empirical composition of the W-IOH precursor is  $\text{WO}_3 \cdot \text{H}_2\text{O} \cdot \text{BA}$ . Fig. 2 shows the TEM and HRTEM images of the W-IOH precursor, the particles of which exhibit plate-like shapes with diameters of  $\sim 50 \text{ nm}$  and a thickness less than  $5 \text{ nm}$ .

### 3.2 Thermal transformation of the W-IOH precursor to $\text{WO}_3$ nanoplates

Considering the above TG result (Fig. 1c), a calcination temperature of  $450^\circ\text{C}$  is selected to thermally transform W-IOH to  $\text{WO}_3$ . As expected, pure  $\text{WO}_3$  sample is obtained after the thermal treatment at  $450^\circ\text{C}$ . Fig. 3a shows the XRD pattern of the as-obtained  $\text{WO}_3$  sample. It is seen that the XRD diffraction peaks associated with the W-IOH precursor (Fig. 1a) completely disappear upon calcination, and some new diffraction peaks, which are perfectly indexed to monoclinic  $\text{WO}_3$ , show up (Fig. 3a). The obvious broadening of diffraction peaks indicates that the obtained  $\text{WO}_3$  particles are nanocrystals with a small size. In addition, the peak broadening behavior also leads to the overlap of some diffraction peaks. For example, the three strongest diffraction peaks [(002), (020) and (200)] of monoclinic  $\text{WO}_3$  cannot be well-resolved for our sample ( $22 < 2\theta < 26^\circ$ ). Fig. 3b shows the Raman spectrum of the obtained  $\text{WO}_3$  material. In the spectrum between  $200$  and  $1200 \text{ cm}^{-1}$  five distinct bands appear at about  $274$ ,  $326$ ,  $618$ ,  $710$  and  $807 \text{ cm}^{-1}$ . The well-defined Raman bands at  $274$ ,  $326$ ,  $710$ , and  $807 \text{ cm}^{-1}$  fall very close to the positions of the four strongest modes of monoclinic  $\text{WO}_3$ .<sup>17</sup> The bands at  $274$  and  $326 \text{ cm}^{-1}$  are assigned to W–O–W bending modes of the bridging oxygen, and the bands at  $710$  and  $807 \text{ cm}^{-1}$  are ascribed to the corresponding stretching modes. The weak shoulder band at  $618 \text{ cm}^{-1}$  can be

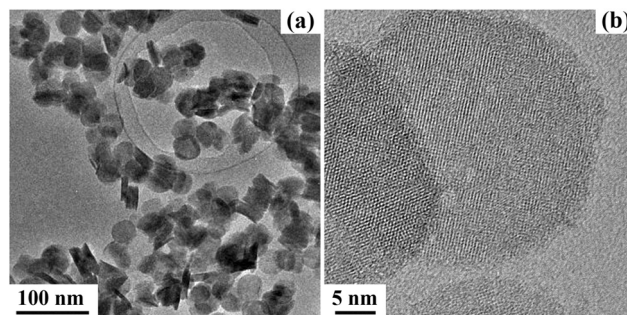


Fig. 2 TEM (a) and HRTEM (b) images of the W-IOH precursor.



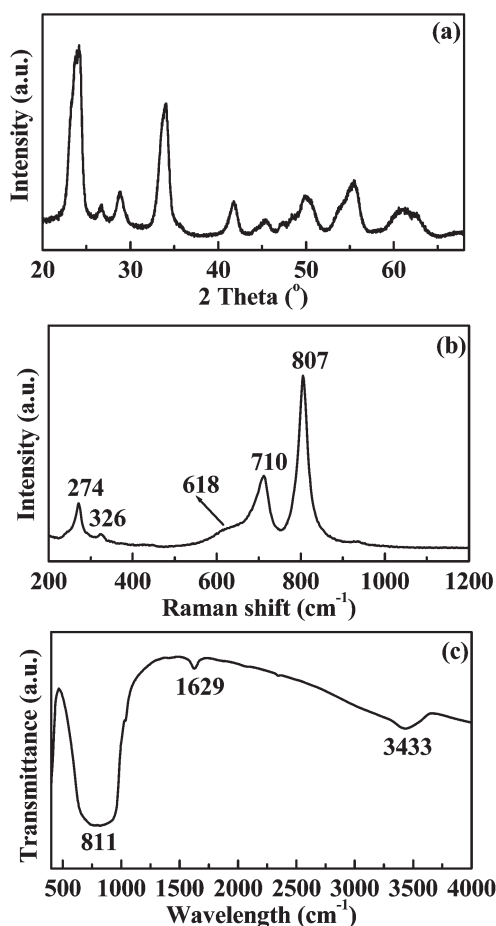


Fig. 3 XRD pattern (a), Raman spectrum (b) and IR spectrum (c) of the solid sample obtained after thermal treatment of the W-IOH precursor at 450 °C.

attributed to the O–W–O stretching vibration that is influenced by the surface OH groups on the surface of the WO<sub>3</sub> particles. The IR spectrum of the obtained WO<sub>3</sub> sample (Fig. 3c) confirms the presence of OH groups because of the appearance of absorption peaks at around 1629 and 3433 cm<sup>-1</sup>. In addition, the total disappearance of the absorption peaks related to W=O bonds and BA molecules (see Fig. 1b) further confirms the complete thermal conversion of the W-IOH precursor to the WO<sub>3</sub> material.

Fig. 4 shows the TEM and HRTEM images of the obtained WO<sub>3</sub> sample. The images reveal that the obtained WO<sub>3</sub> material maintains the plate-like morphology of the W-IOH precursor, and the particle size is about 50–100 nm. Differing from that of the precursor particles (Fig. 2a), the TEM image (Fig. 4a) shows a set of white spots across the whole WO<sub>3</sub> particle. A close inspection of the HRTEM image (Fig. 4b) shows that the WO<sub>3</sub> nanoplate has a convex and concave surface, and the white spots observed in the TEM image are the concave regions. Moreover, this image also reveals that the plate is single crystalline, and the observed lattice spacing is about 0.38 nm, corresponding to the interplanar distance of the (002) reflections for monoclinic WO<sub>3</sub>. It should be pointed out that the unique WO<sub>3</sub> material with an uneven surface is obtained only through the thermal conversion of the W-IOH precursor, and to our knowledge, no other

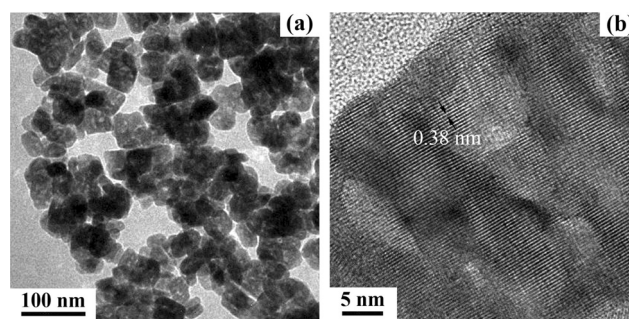


Fig. 4 TEM (a) and HRTEM (b) images of the solid sample obtained after thermal treatment of the W-IOH precursor at 450 °C.

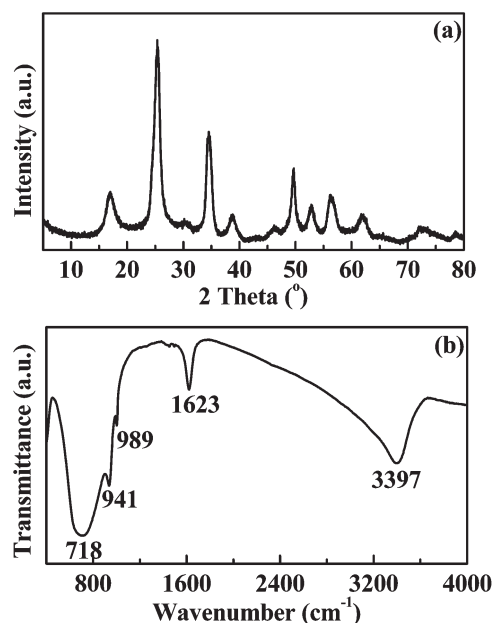


Fig. 5 XRD pattern (a) and IR spectrum (b) of the sample (WO<sub>3</sub>·H<sub>2</sub>O) obtained after UV-irradiation of the W-IOH precursor at room temperature.

synthetic techniques have been successful in achieving similar WO<sub>3</sub> products.

To determine the role of the inorganic–organic hybrid precursor (W-IOH) in the creation of an uneven surface on the WO<sub>3</sub> nanoplates, a light-driven approach<sup>14</sup> was used to extract the organic component (benzene alcohol) from the W-IOH, and then the obtained solid sample was thermally converted to the other WO<sub>3</sub> sample. UV-irradiation of the W-IOH precursor was performed at room temperature in water without deliberate addition of any organic/inorganic species. Fig. 5 presents the XRD pattern and the IR spectrum of the obtained solid product after the UV-irradiation of the W-IOH precursor. It is seen that the XRD diffraction pattern and IR absorption spectrum for the solid product obtained after the UV-irradiation are very different from those for the W-IOH precursor (Fig. 1). Obviously, the XRD peaks associated with the self-assembly between the BA molecules and WO<sub>3</sub>·H<sub>2</sub>O disappear, and the new diffraction peaks in Fig. 6a correspond well to those of WO<sub>3</sub>·H<sub>2</sub>O. The IR absorption

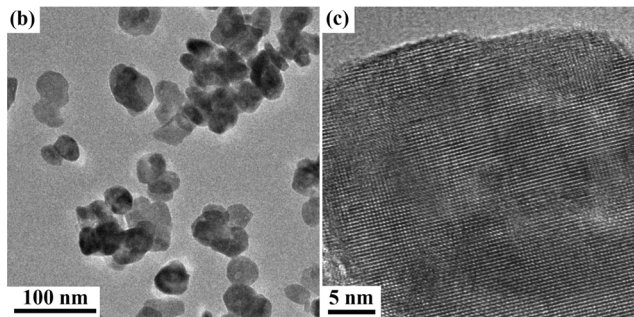
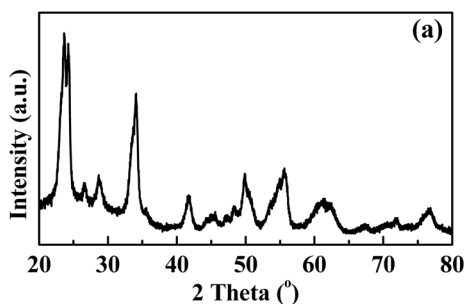


Fig. 6 XRD pattern (a), TEM (b) and HRTEM (c) images of the sample ( $\text{WO}_3$ ) obtained after thermal treatment of  $\text{WO}_3 \cdot \text{H}_2\text{O}$  at  $450^\circ\text{C}$ .

bands for BA molecules (Fig. 1b) also completely disappear, whereas the IR absorption bands related to O–W–O ( $718\text{ cm}^{-1}$ ), W=O ( $941, 989\text{ cm}^{-1}$ ) and OH groups ( $1623, 3397\text{ cm}^{-1}$ ) remain. The X-ray diffraction and the IR spectroscopy indicate that the organic component has been successfully removed from the W-IOH precursor upon UV-irradiation. Indeed, benzyl alcohol has been detected in the aqueous phase through gas chromatography after the UV irradiation of the W-IOH precursor in water, and benzyl alcohol is believed to arise from the removal of the organic component in the W-IOH material. Using the benzyl alcohol-free solid product ( $\text{WO}_3 \cdot \text{H}_2\text{O}$ ) obtained after the UV-irradiation as the precursor, another  $\text{WO}_3$  sample (see XRD pattern in Fig. 6a) is also formed through a simple thermal treatment at  $450^\circ\text{C}$ . The TEM and HRTEM images (Fig. 6a and 6b) reveal that the resultant  $\text{WO}_3$  nanoparticles exhibit a relatively flat surface. This observation demonstrates that the presence of the organic component (benzene alcohol) in the W-IOH precursor is very important for the creation of an uneven surface on  $\text{WO}_3$  nanoplates. The oxidative decomposition of benzene alcohol in the W-IOH precursor during the formation of  $\text{WO}_3$  leads to an acute local structural collapse and/or rearrangement, and thus an uneven surface structure is formed. On the contrary, the dehydration of  $\text{WO}_3 \cdot \text{H}_2\text{O}$  to  $\text{WO}_3$  only causes a relatively moderate structure change, and therefore a flat (even) surface structure is obtained.<sup>18</sup> For clarity, the two different  $\text{WO}_3$  formation processes using the W-IOH precursor are schematically shown in Fig. 7.

### 3.3 Sensing performance of $\text{WO}_3$ nanoplates

Because surface roughness in nanostructures can dramatically influence the amount of surface active sites, it is expected that the unique uneven surface of the  $\text{WO}_3$  nanoplates would bring about better gas sensing performance. For comparison, three gas

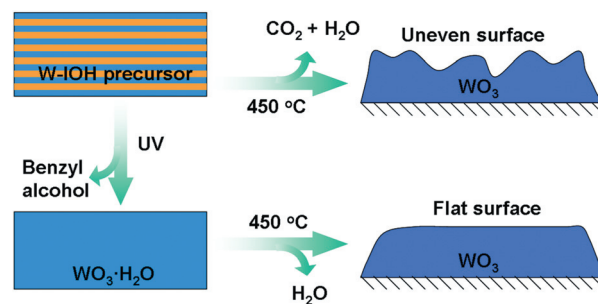


Fig. 7 Schematic diagram showing the two different  $\text{WO}_3$  formation processes using the W-IOH precursor.

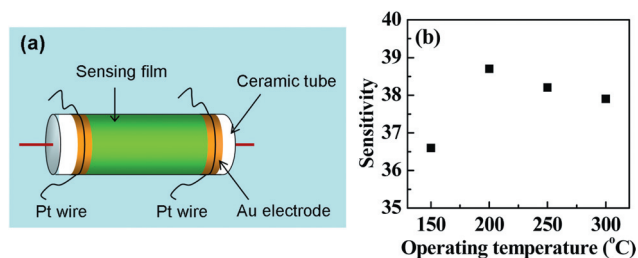


Fig. 8 (a) Schematic diagram showing the structure of a typical gas sensor; (b) sensitivity of the sensor based on the  $\text{WO}_3$ -uneven sample as a function of the operating temperature for the detection of acetone with a concentration of 500 ppm.

sensors were fabricated from the  $\text{WO}_3$  nanoplates with an uneven surface ( $\text{WO}_3$ -uneven), the  $\text{WO}_3$  nanoplates with a flat surface ( $\text{WO}_3$ -flat) and the commercially available  $\text{WO}_3$  sample (com- $\text{WO}_3$ ). A typical sensor was fabricated conveniently by pasting a viscous slurry of the  $\text{WO}_3$  material onto a ceramic tube with a diameter of 1 mm and a length of 4 mm, which was positioned with a pair of Au electrodes and four Pt wires on both ends of the tube (Fig. 8a). A Ni–Cr alloy coil through the tube was employed as a heater to control the operating temperature. The optimal operating temperature of the sensor based on the  $\text{WO}_3$ -uneven sample was determined by testing 500 ppm acetone at different temperatures. As revealed in Fig. 8b, the  $\text{WO}_3$  sensor shows the highest sensitivity toward acetone at  $200^\circ\text{C}$ . Accordingly,  $200^\circ\text{C}$  is believed to be the optimal operating temperature for the detection of acetone, and this operating temperature was applied in all the sensing tests hereinafter. The sensor sensitivity is defined as the ratio  $R_a/R_g$ , where  $R_a$  and  $R_g$  are the electrical resistances of the sensor in atmospheric air and in the testing gas, respectively. The response and recovery times are defined as the times taken by the sensor to achieve 90% of the total resistance change in the case of adsorption and desorption, respectively.

Fig. 9a and 9b show the dynamic response–recovery curves of the  $\text{WO}_3$ -uneven sensor with increasing acetone and ethanol concentrations, respectively. It is seen that the sensor has a wide response range for both acetone and ethanol from 5 to 500 ppm. The sensitivity increases significantly with increasing acetone/ethanol concentration. For acetone concentrations of 5, 10, 20, 50, 100, 200, and 500 ppm, the sensitivities are about 2.3, 3.1, 4.2, 8.5, 11.2, 19.6, and 38.7, respectively. For ethanol

concentrations of 5, 10, 20, 50, 100, 200, and 500 ppm, the sensitivities are about 2.6, 3.3, 4.5, 6.1, 8.5, 10.1, and 13.4, respectively. For comparison, the sensing performances of WO<sub>3</sub>-flat and com-WO<sub>3</sub> have also been tested. Fig. 9c and 9d show the gas concentration-dependent sensitivities of the sensors based on the three materials. It is obvious that the sensors based on the WO<sub>3</sub>-uneven and WO<sub>3</sub>-flat materials exhibit sensitivities distinctly higher than that based on the commercial WO<sub>3</sub> (com-WO<sub>3</sub>), and the performance of WO<sub>3</sub>-uneven in terms of sensitivity is superior to that of WO<sub>3</sub>-flat, especially for the acetone detection. The sensitivity of WO<sub>3</sub>-uneven is about 2.9 times as high as that of WO<sub>3</sub>-flat (7.3 times com-WO<sub>3</sub>) in the presence of 500 ppm acetone. In comparison with a highly sensitive hollow WO<sub>3</sub> material reported previously,<sup>12</sup> the WO<sub>3</sub>-uneven material we obtained also exhibits a much better sensing performance. For instance, the sensitivity values for the hollow WO<sub>3</sub> material are 13.5 and 6.14, whereas the corresponding values for the WO<sub>3</sub>-uneven material are about 38.7 and 13.4 in the presence of 500 ppm acetone and ethanol, respectively.

Fig. 9c and 9d demonstrate that WO<sub>3</sub>-flat and com-WO<sub>3</sub> exhibit very similar sensitivities for acetone and ethanol detection. Similar sensing behavior to ethanol and acetone has been observed in many oxide-based sensing investigations.<sup>19</sup> In contrast with these two materials, the WO<sub>3</sub>-uneven material shows a much higher sensitivity for acetone than for ethanol detection at the high gas concentration (>50 ppm). The selective acetone detection of the WO<sub>3</sub>-uneven sensor is further confirmed by

comparing responses of the WO<sub>3</sub>-uneven sensor to acetone, ethanol, methanol, hydrogen, carbon monoxide, ethylene and methane. As shown in Fig. 10, the WO<sub>3</sub>-uneven sensor is less sensitive to ethanol, methanol and hydrogen, and totally insensitive to carbon monoxide, ethylene and methane.

Response and recovery times are also critical for a gas sensor. From Fig. 9a and 9b, it is seen that the response and recovery times of the WO<sub>3</sub>-uneven sensor are fast for the detection of acetone and ethanol vapors. For acetone detection, the time of response is less than 3 s, and the recovery time is less than 6 s.

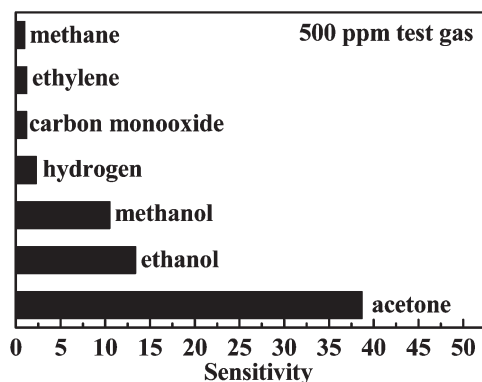


Fig. 10 Sensitivity comparison of the WO<sub>3</sub>-uneven material in the presence of 500 ppm test gas.

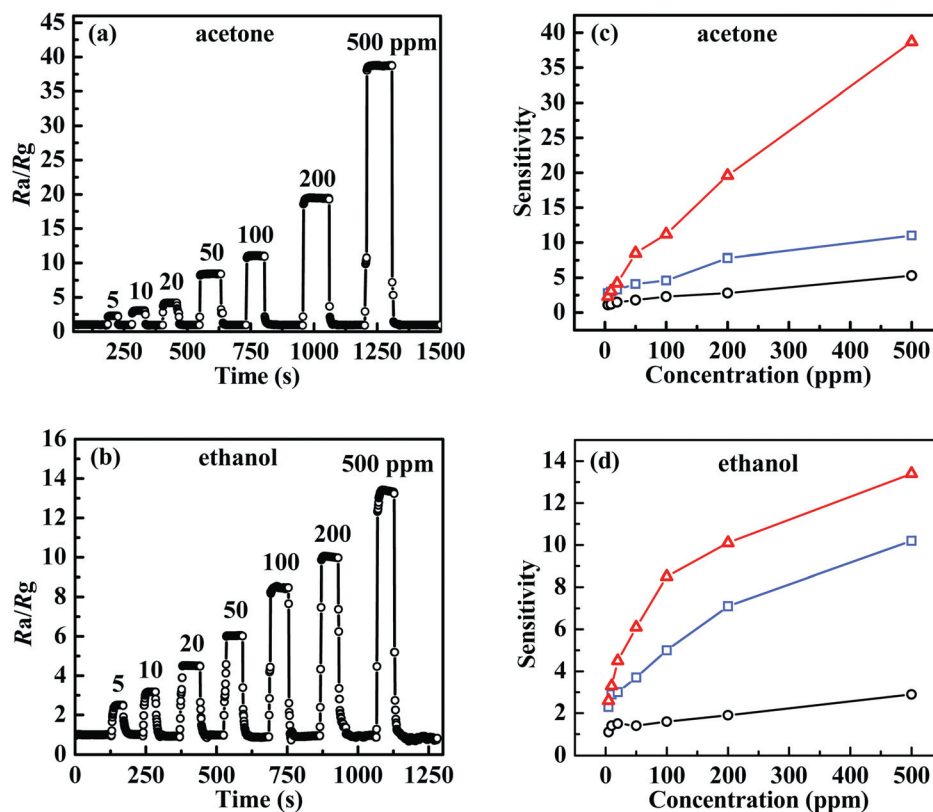
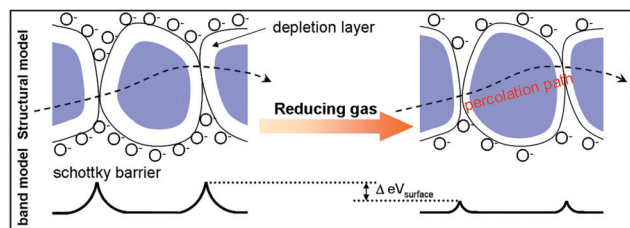


Fig. 9 Dynamic response-recovery curves of the sensor based on the WO<sub>3</sub>-uneven sample for (a) acetone and (b) ethanol detection; and the corresponding comparisons (c), (d) of the gas concentration-dependent sensitivities of WO<sub>3</sub>-uneven (red line), WO<sub>3</sub>-flat (blue line) and com-WO<sub>3</sub> (black line).





**Fig. 11** Schematic representation of the sensing mechanism of the  $\text{WO}_3$  material.

For ethanol detection, the times of response and recovery are less than 6 s. From the above sensing results, it is concluded that the  $\text{WO}_3$ -uneven nanomaterial is very promising for the fabrication of an acetone sensor because of its high sensitivity, obvious selectivity and fast response and recovery.

Taking into account the fact that  $\text{WO}_3$ -uneven and  $\text{WO}_3$ -flat possess a plate-like morphology and a particle size much smaller than the commercially available  $\text{WO}_3$  sample (see SEM images of com- $\text{WO}_3$  in Fig. S2†) and the former two materials exhibit distinctly higher sensitivities than the latter, it is clear that the particle size and morphology play an important role in determining the gas sensing performance of  $\text{WO}_3$ .<sup>12,13</sup> However,  $\text{WO}_3$ -uneven and  $\text{WO}_3$ -flat have the same crystal structure (see Fig. 3a and 6a), similar plate-like shapes (see Fig. 4 and 6) and similar surface areas ( $26.4 \text{ m}^2 \text{ g}^{-1}$  for  $\text{WO}_3$ -uneven;  $24.8 \text{ m}^2 \text{ g}^{-1}$  for  $\text{WO}_3$ -flat), and thus these factors cannot be the reason behind the enhanced sensing performance of  $\text{WO}_3$ -uneven versus  $\text{WO}_3$ -flat. Considering that the biggest structural difference between  $\text{WO}_3$ -uneven and  $\text{WO}_3$ -flat is its surface structure, the excellent sensing performance of the  $\text{WO}_3$ -uneven material, therefore, should be attributed to the uneven surface structure in comparison with the  $\text{WO}_3$ -flat material. This unique structural feature (uneven surface) for the  $\text{WO}_3$  nanoplates leads to an enhanced number of available reactive sites, thus improving the gas sensing performance of the material significantly.

The gas sensing behavior of  $\text{WO}_3$  is generally ascribed to the interaction of surface chemisorbed oxygen and the gas molecules to be detected.<sup>8</sup> Fig. 11 shows the schematic representation of the sensing mechanism of the  $\text{WO}_3$  material. The oxygen molecules in air are chemisorbed on the  $\text{WO}_3$  surface and function as electron acceptors. The individual chemisorbed oxygen extracts electrons from the conduction band of  $\text{WO}_3$ , leading to the creation of a potential barrier and thus a high resistance state. When the sensor is exposed to a reductive gas (such as acetone) at moderate temperature, the gas reacts with the surface oxygen species, resulting in a decrease of the amount of adsorbed oxygen. As a consequence, the height of the potential barrier is reduced, and the resistance of the whole sensing layer decreases significantly. The increase in the number of available reactive sites enhances the interaction of surface chemisorbed oxygen and the gas molecules to be detected, thereby promoting the performance of the gas sensor. For the  $\text{WO}_3$ -uneven material, the combination of an ultrathin plate-like morphology with an uneven surface structure provides not only a high surface area but also rich atomic steps with a concave surface topology.<sup>20</sup> The abundant atomic steps result in a significantly increased

amount of reactive sites which play an important role in the gas sensing process of  $\text{WO}_3$ .

## 4. Conclusion

A benzyl alcohol-mediated nonaqueous synthetic route has been found to result in the formation of a W-containing inorganic–organic nanohybrid with a plate-like morphology. By using this inorganic–organic nanohybrid as a precursor, a new  $\text{WO}_3$  nanoplate material with an uneven surface is directly obtained via a simple thermal treatment process. The presence of an organic component (benzene alcohol) in the W-IOH precursor has proved to be very important for the creation of the uneven surface on  $\text{WO}_3$  nanoplates. Furthermore, investigations into the gas sensing properties of the as-prepared  $\text{WO}_3$  reveal that this nanomaterial is promising for the fabrication of an acetone sensor because of its high sensitivity, obvious selectivity and fast response and recovery for acetone detection, and the uneven surface structure besides the particle size and morphology is responsible for the enhancement of the gas sensing performance. Our results further demonstrate that the inorganic–organic nanohybrids are efficient precursors for the preparation of inorganic nanomaterials with unique morphologies and textures, which may lead to markedly enhanced functionalities.

## Acknowledgements

This work was financially supported by the National Basic Research Program of China and the National Natural Science Foundation of China.

## Notes and references

- 1 M. Antonietti, M. Niederberger and B. Smarsly, *Dalton Trans.*, 2008, 18; N. Pinna, *J. Mater. Chem.*, 2007, **17**, 2769; H.-B. Yao, M.-R. Gao and S.-H. Yu, *Nanoscale*, 2010, **2**, 323; X.-X. Zou, G.-D. Li, M.-Y. Guo, X.-H. Li, D.-P. Liu, J. Su and J.-S. Chen, *Chem.-Eur. J.*, 2008, **14**, 11123; X. Huang, M. Roushan, T. J. Emge, W. Bi, S. Thiagarajan, J.-H. Cheng, R. Yang and J. Li, *Angew. Chem., Int. Ed.*, 2009, **48**, 7871; H. R. Heulings IV, X. Huang and J. Li, *Nano Lett.*, 2001, **1**, 521.
- 2 W. Yao, S.-H. Yu, X. Huang, J. Jiang, L. Q. Zhao, L. Pan and J. Li, *Adv. Mater.*, 2005, **17**, 2799; S. Yu and M. Yoshimura, *Adv. Mater.*, 2002, **14**, 296; L. Fan, H. Song, H. Zhao, G. Pan, H. Yu, X. Bai, S. Li, Y. Lei, Q. Dai, R. Qin, T. Wang, B. Dong, Z. Zheng and X. Ren, *J. Phys. Chem. B*, 2006, **110**, 12948; Y. Dong, Q. Peng and Y. Li, *Inorg. Chem. Commun.*, 2004, **7**, 370.
- 3 Q. Gao, P. Chen, Y. Zhang and Y. Tang, *Adv. Mater.*, 2008, **20**, 1837; P. J. Hagerman, D. Hagerman and J. Zubieta, *Angew. Chem., Int. Ed.*, 1999, **38**, 2638; B. Yan, Y. Xu, N. K. Goh and L. S. Chia, *Chem. Commun.*, 2000, 2169.
- 4 N. Pinna, G. Garnweitner, P. Beato, M. Niederberger and M. Antonietti, *Small*, 2005, **1**, 112; M. Karmaoui, L. Mafta, R. A. S. Ferreira, J. Rocha, L. D. Carlos and N. Pinna, *J. Phys. Chem. C*, 2007, **111**, 2539; R. A. S. Ferreira, M. Karmaoui, S. S. Nobre, L. D. Carlos and N. Pinna, *ChemPhysChem*, 2006, **7**, 2215; M. Karmaoui, R. A. S. Ferreira, A. T. Mane, L. D. Carlos and N. Pinna, *Chem. Mater.*, 2006, **18**, 4493.
- 5 Y. Yu, J. Zhang, X. Wu, W. Zhao and B. Zhang, *Angew. Chem., Int. Ed.*, 2012, **51**, 897; X. Wu, Y. Yu, Y. Liu, Y. Xu, C. Liu and B. Zhang, *Angew. Chem., Int. Ed.*, 2012, **51**, 3211.
- 6 J. W. Jang, S. H. Choi, J. S. Jang, J. S. Lee, S. Cho and K. Lee, *J. Phys. Chem. C*, 2009, **113**, 20445; J. Liu, Z. Guo, F. Meng, T. Luo, M. Li and J. Liu, *Nanotechnology*, 2009, **20**, 125501; Z.-A. Zang, H.-B. Yao, Y.-X. Zhou, W.-T. Yao and S.-H. Yu, *Chem. Mater.*, 2008, **20**, 4749.
- 7 L.-S. Zhong, J.-S. Hu, L.-J. Wan and W.-G. Song, *Chem. Commun.*, 2008, 1184; X.-X. Zou, G.-D. Li, Y.-N. Wang, J. Zhao, C. Yan,



- M.-Y. Guo, L. Li and J.-S. Chen, *Chem. Commun.*, 2011, **47**, 1066;  
 X. Jiang, Y. Wang, T. Herricksb and Y. Xia, *J. Mater. Chem.*, 2004, **14**, 695; Y. Wang, X. Jiang and Y. Xia, *J. Am. Chem. Soc.*, 2003, **125**, 16176;  
 D. Chen, L. Gao, A. Yasumori, K. Kuroda and Y. Sugahara, *Small*, 2008, **4**, 1813; J. Polleux, A. Gurlo, N. Barsan, U. Weimar, M. Antonietti and M. Niederberger, *Angew. Chem., Int. Ed.*, 2006, **118**, 267.
- 8 M. E. Franke, T. J. Koplín and U. Simon, *Small*, 2006, **2**, 36.
  - 9 W. H. Brattein and J. Bardeen, *Bell Syst. Tech. J.*, 1953, **32**, 1; G. Heiland, *Z. Phys.*, 1954, **138**, 549; T. Seiyama, A. Kato, K. Fujiishi and M. Nagatami, *Anal. Chem.*, 1962, **34**, 1502; T. Seiyama and S. Kagawa, *Anal. Chem.*, 1966, **38**, 1069.
  - 10 S. Vallejos, T. Stoycheva, P. Umek, C. Navio, R. Snyders, C. Bittencourt, E. Llobet, C. Blackman, S. Moniz and X. Correig, *Chem. Commun.*, 2011, **47**, 565; S. J. Ippolito, S. Kandasamy, K. Kalantar-zadeh and W. Wlodarski, *Sens. Actuators, B*, 2005, **108**, 154; Y. Shimizu, N. Matsunaga, T. Hyodo and M. egashira, *Sens. Actuators, B*, 2001, **77**, 35; M. D'Arienzo, L. Armelao, C. M. Mari, S. Polizzi, R. Ruffo, R. Scotti and F. Morazzoni, *J. Am. Chem. Soc.*, 2011, **133**, 5296; G. N. Chaudhari, A. M. Bende, A. B. Bodade, S. S. Patil and V. S. Sapkal, *Sens. Actuators, B*, 2006, **115**, 297; Q. Xiang, G. F. Meng, H. B. Zhao, Y. Zhang, H. Li, W. J. Ma and J. Q. Xu, *J. Phys. Chem. C*, 2010, **114**, 2049; X. Liu, J. Zhang, T. Yang, X. Guo, S. Wu and S. Wang, *Sens. Actuators, B*, 2011, **156**, 918.
  - 11 L. Wang, A. Teleki, S. E. Pratsinis and P. I. Gouma, *Chem. Mater.*, 2008, **20**, 4794; M. Righettoni, A. Tricoli and S. E. Pratsinis, *Anal. Chem.*, 2010, **82**, 3581; M. Righettoni, A. Tricoli and S. E. Pratsinis, *Chem. Mater.*, 2010, **22**, 3152.
  - 12 X.-L. Li, T.-J. Lou, X.-M. Sun and Y.-D. Li, *Inorg. Chem.*, 2004, **43**, 5442.
  - 13 G. Wang, Y. Ji, X. Huang, X. Yang, P. Gouma and M. Dudley, *J. Phys. Chem. B*, 2006, **110**, 23777; S.-J. Kim, I.-S. Hwang, J.-K. Choi and J.-H. Lee, *Thin Solid Films*, 2011, **519**, 2020; D. Chen, X. Hou, H. Wen, Y. Wang, H. Wang, X. Li, R. Zhang, H. Lu, H. Xu, S. Guan, J. Sun and L. Gao, *Nanotechnology*, 2010, **21**, 035501; C.-Y. Lee, S.-J. Kim, I.-S. Hwang and J.-H. Lee, *Sens. Actuators, B*, 2009, **142**, 236; Z. Xie, Y. Zhu, J. Xu, H. Huang, D. Chen and G. Shen, *CrystEngComm.*, 2011, **13**, 6393; N. V. Hieu, V. V. Quang, N. D. Hoa and D. Kim, *Curr. Appl. Phys.*, 2011, **11**, 657; J. Shi, G. Hu, Y. Sun, M. Geng, J. Wu, Y. Liu, M. Ge, J. Tao, M. Cao and N. Dai, *Sens. Actuators, B*, 2011, **156**, 820.
  - 14 X.-X. Zou, G.-D. Li, K.-X. Wang, L. Li, J. Su and J.-S. Chen, *Chem. Commun.*, 2010, **46**, 2112; X.-X. Zou, G.-D. Li, J. Zhao, P.-P. Wang, Y.-N. Wang, L.-J. Zhou, J. Su, L. Li and J.-S. Chen, *Inorg. Chem.*, 2011, **50**, 9106.
  - 15 J. Polleux, M. Antonietti and M. Niederberger, *J. Mater. Chem.*, 2006, **16**, 3969.
  - 16 M. F. Daniel, B. Desbat, J. C. Lassegues, B. Gerand and M. Figlarz, *J. Solid State Chem.*, 1987, **67**, 235.
  - 17 C. Santato, M. Odziemkowski, M. Ulmann and J. Augustynski, *J. Am. Chem. Soc.*, 2001, **123**, 10639.
  - 18 F. Amano, D. Li and B. Ohtani, *Chem. Commun.*, 2010, **46**, 2769; Y. P. Xie, G. Liu, L. Yin and H.-M. Cheng, *J. Mater. Chem.*, 2012, **22**, 6746.
  - 19 B. L. Zhu, C. S. Xie, W. Y. Wang, K. J. Huang and J. H. Hu, *Mater. Lett.*, 2004, **58**, 624; Z. Jie, H. L. Hua, G. Shan, Z. Hui and Z. J. Gui, *Sens. Actuators, B*, 2006, **115**, 460; H. Gong, Y. J. Wang, S. C. Teo and L. Huang, *Sens. Actuators, B*, 1999, **54**, 232; X.-X. Zou, G.-D. Li, Y.-C. Zou, P.-P. Wang, J. Su, J. Zhao, Y.-N. Wang and J.-S. Chen, *Acta Chim. Sin.*, DOI: 10.6023/a12030002.
  - 20 A. Takai, H. Ataee-Esfahani, Y. Doi, M. Fuziwara, Y. Yamauchi and K. Kuroda, *Chem. Commun.*, 2011, **47**, 7701; S. W. Lee, S. Chen, W. Sheng, N. Yabuuchi, Y. Kim, T. Minami, E. Vescovo and Y. Shao-Horn, *J. Am. Chem. Soc.*, 2009, **131**, 15669.